J Electroceram (2012) 29:171–178
DOI 10.1007/s10832-012-9756-x

Synthesis, crystal structure and ferroelectric properties of $SrBi_2Nb_2O_9$ embedded in a 50 % $Li_2B_4O_7$ glass matrix

E. K. Abdel-Khalek · Shaaban M. Salem · I. Kashif

Received: 4 October 2011 / Accepted: 15 August 2012 / Published online: 23 August 2012

Abstract Transparent glass sample [$50Li_2B_4O_7$–$50(SrO–Bi_2O_3–Nb_2O_5)$] (mol%) was prepared by the melt-quenching technique. The glassy nature of the as-prepared sample was established by Differential scanning calorimetry (DSC). Ferroelectric $SrBi_2Nb_2O_9$ (SBN) embedded in a 50 % $Li_2B_4O_7$ glass matrix was produced by heat-treating the as-prepared sample at 874 K (HT874) for 6 h. The X-ray structural analysis showed that $SrBi_2Nb_2O_9$ crystallizes in the orthorhombic ($A2_1am$) with a=5.5104, b=5.5096 and c= 25.0794 Å. Infrared spectroscopy studies corroborate the observation of $SrBi_2Nb_2O_9$ phase formation. The dielectric properties have been studied in the frequency range of 120 Hz to 100 kHz at various temperatures (300–815 K). The high frequency dielectric constant $\left(\varepsilon_r'\right)$ shows a peak at T_c (743 K). The exponent n(T) and the coefficient A(T) in the Jonscher's expression were found to be minimum and maximum respectively at the Curie temperature (T_c). AC conductivity measurements for present sample were reported.

Keywords Strontium bismuth niobate · Ferroelectric · X-ray diffraction · Dielectric properties

1 Introduction

Recently, Bismuth layer structured ferroelectrics have attracted much attention because they have good structural stability, high Curie temperatures, anisotropic characteristics, and properties suitable for use as memory devices [1, 2]. Bismuth layer is reported to be paraelectric in nature while perovskite unit cell structures are ferroelectric [3]. The general formula of layered perovskites is $[Bi_2O_2]^{2+}[A_{n-1}B_nO_{3n+1}]^{2-}$, where A is in 12-fold coordination, B is in 6-fold coordination and n is an integer ranging from 1 to 5 [4]. SBN ($SrBi_2Nb_2O_9$) is an n= 2 member of the Aurivillius family of the layered ferroelectric oxides [4]. $SrBi_2Nb_2O_9$ (SBN) has attracted much scientific attention due to their fatigue-free properties that make them potentially suitable candidates for application in the nonvolatile ferroelectric random access memory (FE-RAM) [1–3]. Controlled crystallization in glasses has led to the development of glass-ceramic materials with fine-grained nanostructure and specific properties [5]. Much of the work in the field of glass-ceramics has been done on the mechanical and thermal properties. On the other hand, fewer investigations were reported on the high-permittivity glass-ceramics containing a ferroelectric phase, such as $LiNbO_3$ [6, 7] and $SrBi_2Nb_2O_9$ [8, 9]. We have been attempting to fabricate $Li_2B_4O_7$ host glass matrices consisting of $SrBi_2Nb_2O_9$. It is known that the bulk ionic conductivities of SBN (~10^{-7}S/cm) are much higher than those of the perovskite ferroelectrics, e.g., $PbZr_{1-x}Ti_xTi_xO_3$ (~10^{-11}–10^{-10}S/cm) [10]. The existence of electrical conductivity of this magnitude in ferroelectric materials is an undesirable feature, as the dielectric constant measurements do not reflect the real contribution from the lattice, when space charge polarization, triggered by conductivity mechanism, is prevalent [10, 11]. To the best of our knowledge there is no report describing the precise crystal structures of $SrBi_2Nb_2O_9$ embedded in a 50 % $Li_2B_4O_7$ glass matrix. So the purpose of the present paper is to study the ferroelectric $SrBi_2Nb_2O_9$ phase in glass matrix by using X-ray diffraction, Infrared spectroscopy, AC conductivity and dielectric properties. The results are reported in this paper.

E. K. Abdel-Khalek (✉) · S. M. Salem · I. Kashif
Department of Physics, Faculty of Science, Al-Azhar University, Nasr City,
11884 Cairo, Egypt
e-mail: Eid_khalaf0@yahoo.com

2 Experimental

The $50Li_2B_4O_7$-$50(SrO$-Bi_2O_3-$Nb_2O_5)$ (mol%) transparent glass was prepared by the conventional melt quenching

technique. The glass sample under investigation was prepared from reagent grade $Li_2B_4O_7$, SrO, Bi_2O_3 and Nb_2O_5. The batches were ground well and packed into porcelain crucible. An electrical furnace was used for melting this sample. This mixture was melted at 1050–1100 °C for 1 h to yield 20 g of the glass. The melt was poured on to a copper plate and immediately pressed into plates. Strontium bismuth niobate, $SrBi_2Nb_2O_9$ (SBN) nanocrystal embedded in a 50 % $Li_2B_4O_7$ glass matrix was produced by heat-treating (HT) the as-prepared sample in air at 874 K (HT874) during 6 h. The differential scanning calorimetry (DSC) for glass sample was carried out on a SETARAM Labsys™ TG-DSC16 thermal analyser in the 303–1273 K temperature range. X-ray diffraction studies were performed at room temperature (RT) from a Siemens D5000 diffractometer using Cu Kα radiation. Rietveld analysis of the diffraction data was performed using the FULLPROF program. The mean crystallite size of $SrBi_2Nb_2O_9$ was evaluated from X-ray diffraction based on Scherrer's equation. The IR spectrum of the glass–ceramic was recorded at room temperature on a Bruker (Vector 22), single beam spectrometer with a resolution of 2 cm^{-1}. The IR transmission spectrum was recorded using KBr pellets containing 2–5 mg of sample. AC electrical conductivity and dielectric properties of the nanocrystalline glass–ceramic phase will be measured as a function of temperature and frequency. The ac data was collected using electronic RLC bridge type SR 720.

3 Results and discussion

3.1 DSC

Figure 1 shows the DSC curve for the as-prepared glass at heating rate 20 K/min. The glass sample exhibits endothermic minima which represent the glass transition temperature T_g at 721 K. As can be seen from (Fig. 1), also the exothermic peaks (T_{cr1} and T_{cr2}) occurred at 772 (broad and less intense) and 874 K (sharp and more intense) followed by

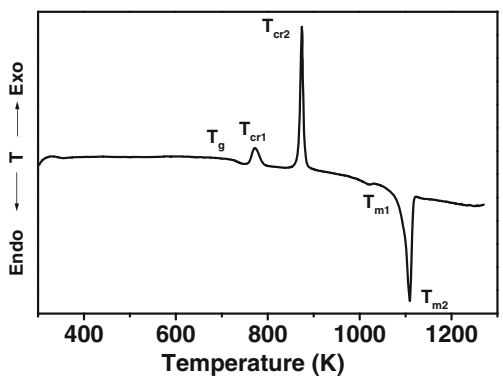

Fig. 1 Differential scanning calorimetry for the as-prepared sample

two endothermic peaks at 1021 and 1108 K. These exothermic peaks are caused by the crystallization of different phases from glass matrix [8, 12], and the two endothermic peaks were related to the melting processes. It is known that the shape of the exothermic peak is strongly influenced by the crystallization mechanism. The broad and sharp exothermic peaks can be attributed to the surface and bulk crystallization, respectively [13].

3.2 X-ray diffraction studies

The XRD pattern corresponding to the as-prepared sample exhibits a broad hump without any distinct peak (Fig. 2 (a)), which confirms the amorphous nature of the sample. The XRD pattern for the HT874 sample (Fig. 2 (b)) shows its single-phase character with the presence of weak diffraction peak at $2\theta = 21.71$, due to the precipitation of very small amount of $Li_2B_4O_7$ [7, 8]. Rietveld refinement of the data reveals that the sample crystallizes in an orthorhombic $SrBi_2Nb_2O_9$ with space group $A2_1am$ consistent with the previously reported results [4, 8]. This suggests the transformation of the SBN from fluorite to perovskite phase [8, 14]. Refined values of the lattice and positional parameters at room temperature are summarized in Table 1. The lattice constants are found to be in excellent agreement with the earlier results [8, 15, 16] within the experimental error. The lattice parameters (a=5.5104, b=5.5096 and c=25.0794 Å) computed based on this pattern are comparable with those reported (a=5.5189, b=5.5154 and c=25.1124 Å) in the literature for a typical polycrystalline SBN phase [16]. The d-spacings, computed from these patterns are in close agreement with those reported in the literature for a polycrystalline SBN phase obtained by conventional solid state reaction route [16]. But there is a noticeable shift in the peak positions towards higher angles than those of the pure powder sample of SBN. This shift can be attributed to the existence of uneven distribution of strain which arising out of the anisotropic growth of SBN crystals in $Li_2B_4O_7$ glass matrix [8, 17]. It is because of the fact that these oxides have a tendency to grow in platy form, which is hindered in the present case by the presence of surrounding viscous glassy phase [8, 17]. The crystallite size obtained at this stage of heating based on Scherrer analyses is about 74 nm. As the growth of SBN nanocrystallites initiates in the glass matrix of $Li_2B_4O_7$, they experience selective compressive pressure effects that are exerted by the surrounding viscous glass matrix. Since SBN has a tendency to grow anisotropically, which is known in the layered materials of the present kind, different planes of the crystal are likely to experience different amounts of strain. In the prototype structure (Fig. 3), Sr is coordinated to 12 oxygen atoms; bismuth is bonded to 5 oxygen atoms, while niobium occupies the MO_6 position in the perovskite layer. In a simple perovskite-type structure,

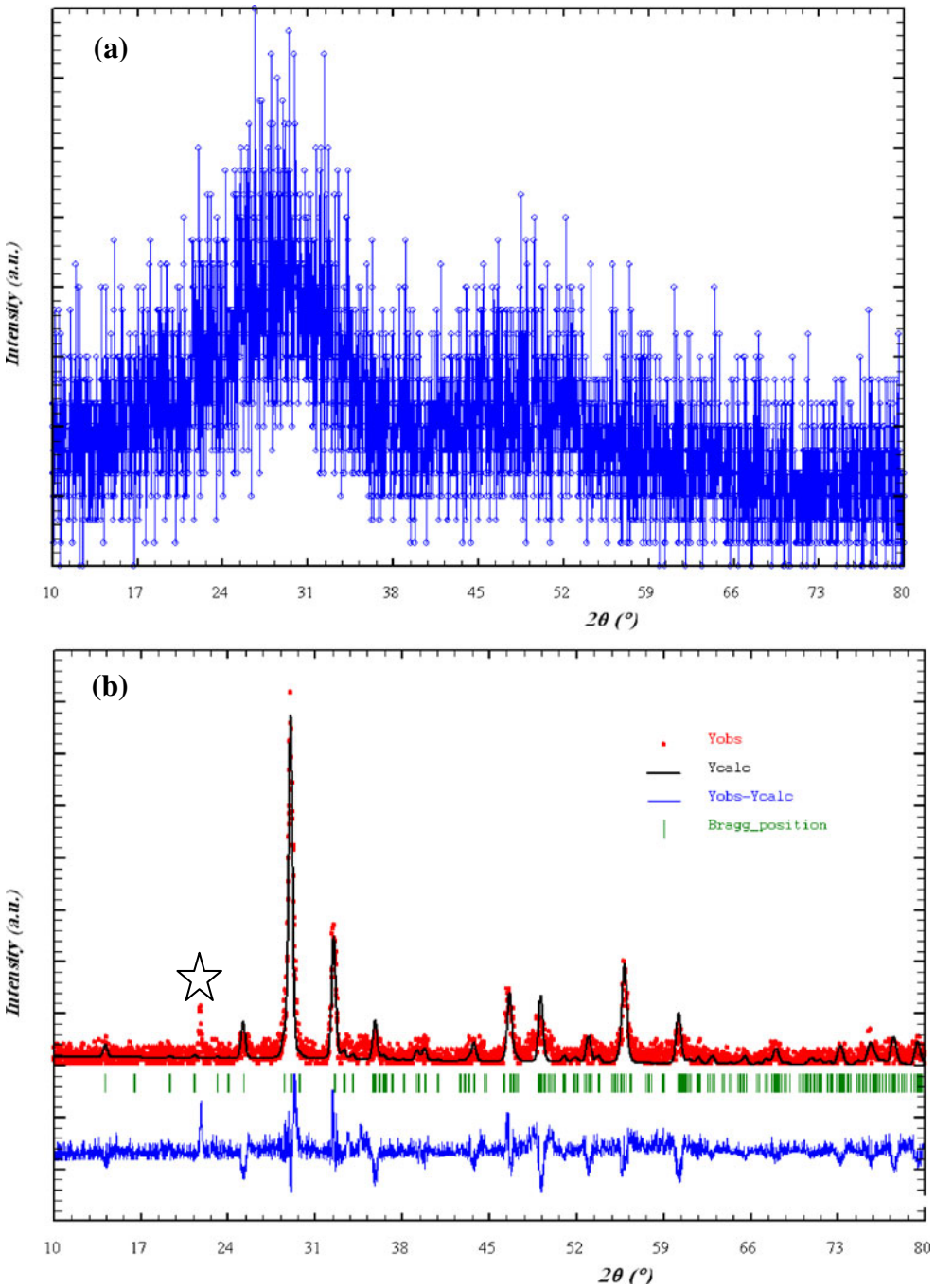

Fig. 2 (**a**) The XRD pattern for the as-prepared sample. (**b**) Rietveld plot of X-ray diffraction (XRD) pattern for the HT874 sample. *Red dots* indicate the experimental data and the black lines overlapping them indicate calculated profiles. The *lowest curve* shows the difference between experimental and calculated patterns. The *vertical bars* in green are the expected Bragg's positions. The peak with star is attributed to the very small amount of $Li_2B_4O_7$

it is expected that the O–Nb–O chains are interrupted by $[Bi_2O_2]^{2+}$ layers not only along the c axis but also by translation of the perovskite plane perpendicular to the c axis relative to the neighboring perovskite planes [16]. On the other hand, unbroken O–Nb–O chains are present in the plane perpendicular to the c axis.

3.3 Infrared spectral studies

Figure 4 shows the IR transmission spectrum for the HT sample recorded in the 1800–460 cm^{-1} region. The vibration modes of the borate network are mainly active in three IR spectral regions (i) in the region 1200–1600 cm^{-1}; (ii) in the region 800–1200 cm^{-1} and (iii) in the region 600–800 cm^{-1}. The first region of bands is attributed to the stretching relaxation of the B–O bond of the trigonal BO_3 units while the second region of bands is attributed to BO_4 units and the third region of bands is due to the bending of B–O–B linkages in the borate network [8, 18, 19]. From Fig. 4 we see eight IR bands. The bands at 548, 619 and 787 cm^{-1}, are assigned to the formation of the NbO_6 octahedra in SBN. This suggests that the perovskite SBN phase

Table 1 Refinement parameters of $SrBi_2Nb_2O_9$ embedded in a $Li_2B_4O_7$ glass matrix at room temperature

Lattice constants	Atom	Site	Lattice coordinate			Reliability factor
			x	*y*	z	
a=5.5104 Å	Sr	4*a*	0	0.24216	0	
b=5.5096 Å	Bi	8*b*	0.50890	0.73116	0.20110	χ^2=1.90
c=25.079 Å	Nb	8*b*	0.49800	0.75200	0.41340	
	O(1)	4*a*	0.43537	0.13767	0	
	O(2)	8*b*	0.44337	0.72467	0.34100	
	O(3)	8*b*	0.71137	19.9316	0.25000	
	O(4)	8*b*	0.63295	1.05434	0.08717	
	O(5)	8*b*	0.68895	1.06334	0.57297	

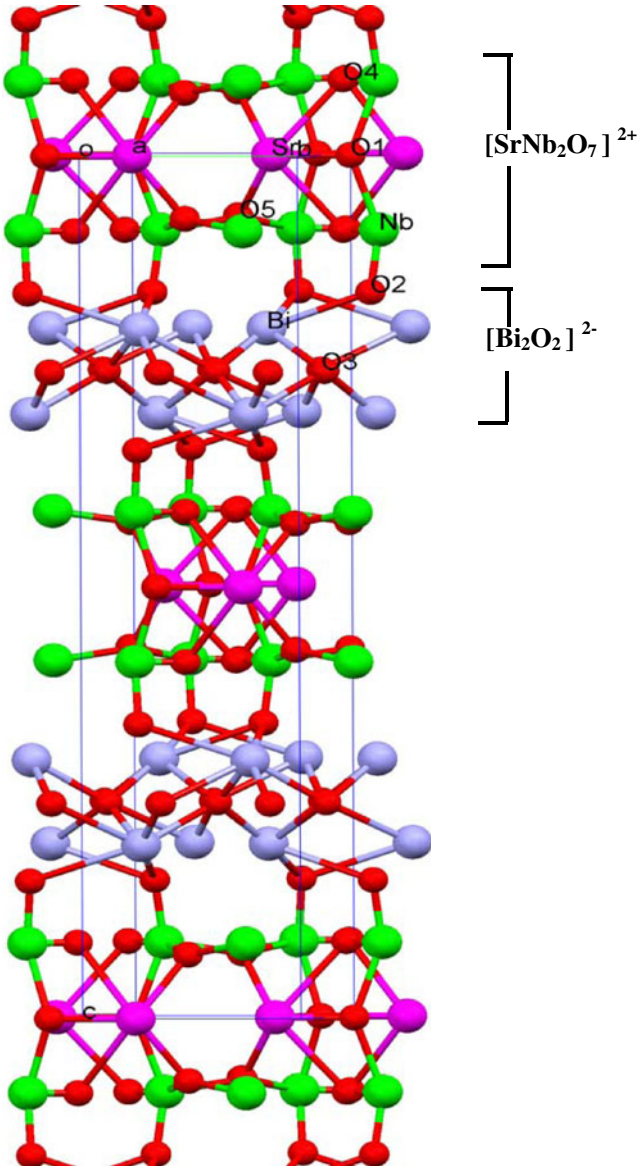

Fig. 3 The Crystal structure of $SrBi_2Nb_2O_9$ showing the alternate $[Bi_2O_2]^{2+}$ and $[SrNb_2O7]^{2-}$ layers. The *line* represents the unit cell

could be obtained by heat-treating the representative glass sample at 874 K for 6 h. The strong modes at 1368, 1143, 987, 904 and 691 (see Fig. 4) are very indicative of the presence of the crystalline phase [20]. The band at 1368 cm^{-1} is assigned to the stretching vibrations of the B–O of trigonal $(BO_3)^{3-}$ units in pyroborates [21]. The prominent bands at 1143 and 987 cm^{-1} are identified with the vibration of the boroxol rings and B-O bond stretching of BO_4 units, respectively [8, 22]. The band at 904 cm^{-1} is attributed to bending vibration of B-O-B bridges of the boron–oxygen network and the band at around 691 cm^{-1} is attributed to bending vibration of pentaborate units [8, 22].

3.4 Dielectric studies

Usually, electronic, ionic, dipolar and space charge polarizations contribute to the dielectric constant (ε_r'). Figure 5 shows the dielectric constants as a function of temperature for the heat-treated (874 K/6 h) sample at various frequencies. For the present sample, a transition in dielectric constant at their respective Curie temperature (T_c) is observed at all the frequencies. The dielectric constants at low temperatures for the

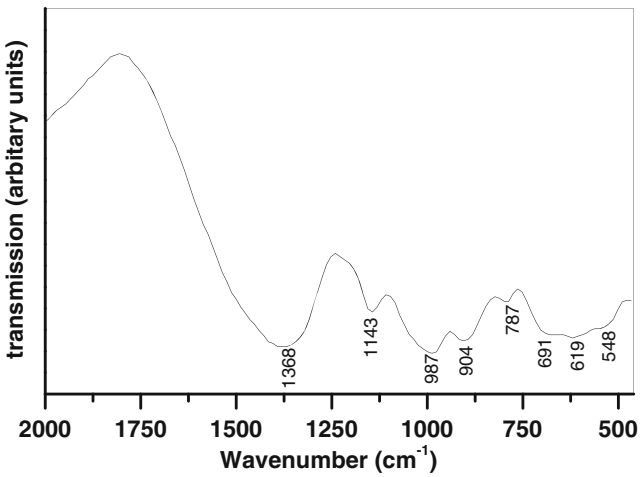

Fig. 4 Infrared transmission spectrum for the HT874 sample

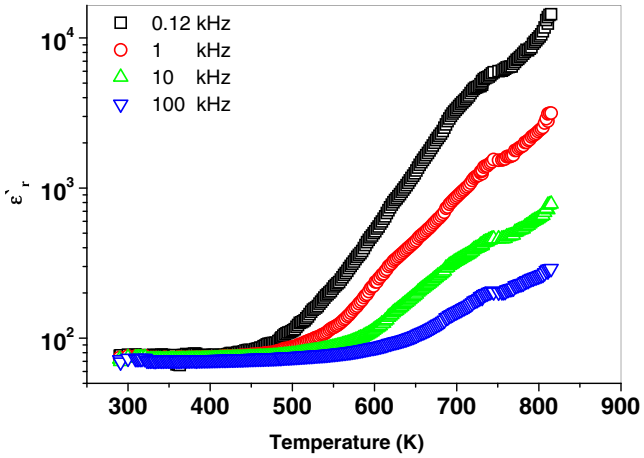

Fig. 5 Variation of ε_r', with temperature for the HT874 sample

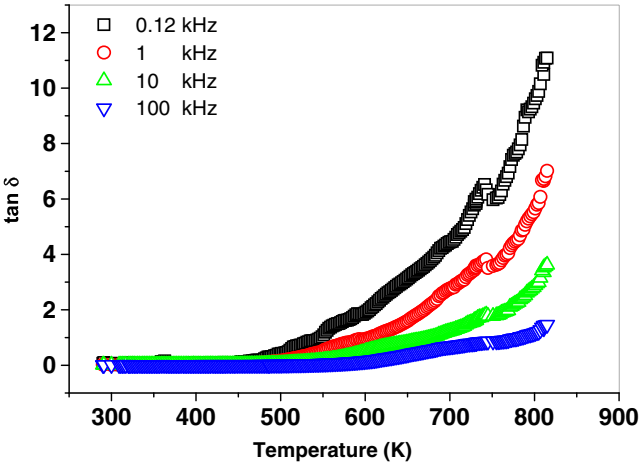

Fig. 6 Variation of tan δ, with temperature for the HT874 sample

sample are also found to be the same regardless of the signal frequencies. The low frequency dielectric dispersion at high temperatures is observed in the sample. It is known that the SBN embedded in a 50 % $Li_2B_4O_7$ glass matrix is not perfectly stoichiometric, but contains a certain amount of inherent defects (e.g. oxygen vacancies). Many investigations of Pb $(Zr,Ti)O_3$ have indicated that the defects such as oxygen vacancies act as space charge which plays an important role in the electrical polarization of perovskite materials [23, 24]. The oxygen vacancy induced polarization becomes dominant at high temperatures and at low frequencies [24]. This explains the significantly enhanced dielectric constant at low frequency (120 and 10 kHz) and high temperatures, observed in the present sample. However, the dispersion at higher frequencies (100 kHz) in the entire temperature range (300–815 K) covered in the present investigations is not significant, suggesting that this phenomenon at low frequencies is coupled with space charge effects. The dielectric loss (tan δ) as a function of temperature for the heat-treated (874 K/6 h) sample at various frequencies is shown in (Fig. 6). The source of dielectric loss in insulating ceramics is space charge polarization/domain wall relaxation [25]. The presence of defects like oxygen vacancies which act as space charge and contribute to the electrical polarization of perovskite materials, can thus be related to the dielectric loss. In the ferroelectric to paraelectric transition region, near T_c (743 K) the dispersion is remarkably high. The ε_r' and tan δ values at 100 kHz and at 300 K are respectively 73 and 0.012, while at T_c these are 205 and 0.85. The high value of tan δ or in other words high ionic conductivity associated with SBN at T_c suggests that there could be a coupling between space charge and ferroelectricity [26]. Figure 7(a) and (b) shows the frequency dependence of ε_r' and ε_r'' of the dielectric constant on a log–log scale at various temperatures for the heat-treated (874 K/6 h) sample respectively. From this Fig. it can be seen that ε_r' and ε_r'' show strong dispersions at low frequencies and it is affected by the temperature change. This result is attributed to the low frequency space charge accumulation effect [26]. This strong dispersions in ε_r' and ε_r'' appear to be a common feature in ferroelectrics associated with non-negligible ionic conductivity and is referred to as the low frequency dielectric dispersion [26–29]. The dispersion in the case of ε_r'' is stronger than ε_r' in this sample. In the range of higher frequencies the weak dispersion of ε_r' suggests that the dispersion is coupled with the space charge carriers. Such strong dispersion in both ε_r' and ε_r'' seems to be a common feature of ferroelectrics with good ionic conductivity [26, 30]. The low frequency slope of the curve log ε_r'' vs. log f is close to −1 indicating the predominance of the dc conduction in this frequency region [26]. In order to understand the influence of the electric conductivity on the ferroelectric properties, the obtained data were plotted as a function of frequency at a few numbers of high temperatures to represent a variation in the real part of the ac conductivity (σ_{ac}) as shown in (Fig. 8). It can be seen that the plateau-like of conductivity, i.e. frequency independent values of conductivity, corresponding to the dc conductivity, was observed in the low frequency region at high temperatures. In the higher frequency region, the strong dispersion of electric conductivity was observed and the changes of σ(ω) in this region can be described as proportional to ω^n, where ω is angular frequency and n is the parameter depending on the temperature. The character of these changes does not depend on the temperature. Although with the increase in temperature it was noted that the range of frequency where dispersion occurs moved to higher frequencies. A similar tendency was observed for polycrystalline SBN phase obtained by conventional solid state reaction [26]. The conductivity spectra for the sample obey Jonscher's law, and ac conductivity is found to vary with angular frequency ω [31].

$$\sigma = \sigma_o + A\omega^n \quad (1)$$

where σ_o is the dc conductivity, A is the temperature dependent parameter and n is found to take values between 0 and 1.

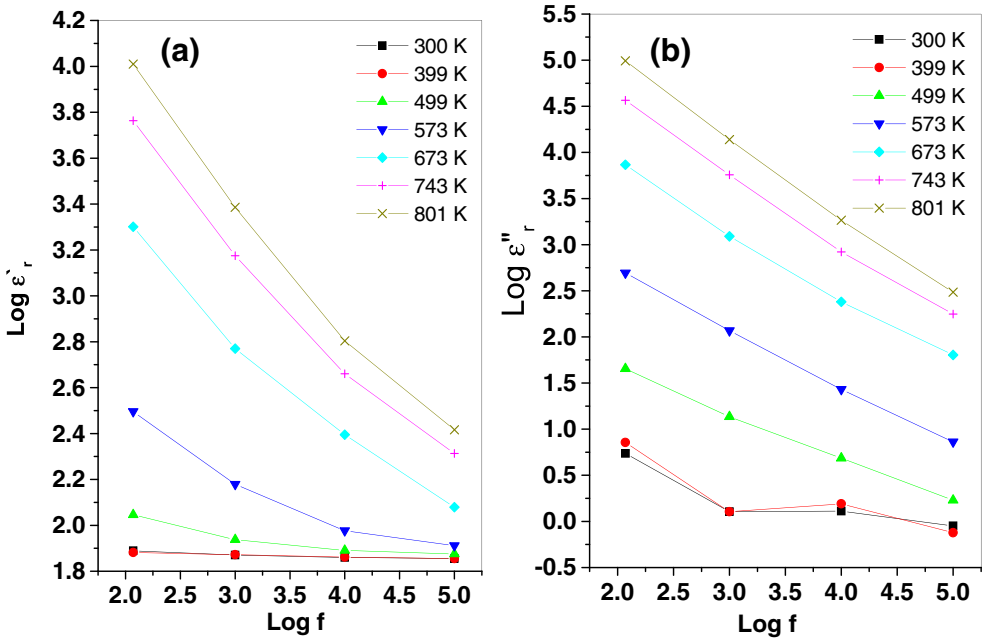

Fig. 7 The frequency dependence of (**a**) ε_r' and (**b**) ε_r'' on a log–log scale at various temperatures for the HT874 sample

The interaction between the charge carriers participating in the polarisation process is characterised by the parameter n (the lower the n value the stronger is the ion–ion coupling [33]). The value of n calculated from the high frequency region decreases as the temperature increases and attains a minimum near T_c and subsequently it increases with further increase in temperature. The observed minimum at T_c implies the strong interaction between the charge carriers and the lattice. The Arrhenius plot derived from the conductivity values at different temperatures at 120 Hz is shown as the inset in Fig. 8. The activation energy calculated from this plot is 0.92 eV and this value is close to the ionic conduction resulting from the mobile oxygen ion vacancies and found to be in agreement with the earlier reports [10]. The complex dielectric constant as a function of the radian frequency $\omega=2\pi f$ in accordance with the Jonscher's power law is given by the following relation.

$$\varepsilon^* = \varepsilon_r' - j\varepsilon_r'' = \varepsilon_\infty + \sigma/j\varepsilon_0\omega + (a_0(T)/\varepsilon_0)\left(j\omega^{n(T)-1}\right) \tag{2}$$

where ε_∞ is the 'high frequency' value of the dielectric constant, σ is the dc conductivity, n(T) is the temperature-dependent exponent and $a_0(T)$ can be given as A(T)L/S, where S and L are the area and the thickness of the sample respectively [12, 26]. Hence the real (ε_r') and imaginary (ε_r'') parts of the complex dielectric constant could be calculated from the following formulas:

$$\varepsilon_r' = \varepsilon_\infty + a_0(T)/\varepsilon_0 \sin(n(T)\pi/2)\omega^{n(T)-1} \tag{3}$$

$$\varepsilon_r'' = \sigma/\varepsilon_0\omega + a_0(T)/\varepsilon_0 \cos(n(T)\pi/2)\omega^{n(T)-1} \tag{4}$$

where the first term in Eq. 3 determines the lattice response and that in the Eq. 4 corresponds to the dc conduction part, while the second part in both the equations describes the contribution of space charge carriers to the observed permittivity of the sample. The dielectric constant ε_r' as a function of temperature and frequency (Figs. 5 and 7(a)) could be explained by Eq. 3. For low frequencies the charge carrier term $a_0(T)/\varepsilon_0 \sin(n(T)\pi/2)\omega^{n(T)-1}$ becomes dominant and the contribution from ε_∞ can be neglected. Therefore, for a constant n, Eq. 3 gives the linear characteristic with the slope n-1 in the ε_r' and frequency on the log–log scale. The charge carriers fail to respond to the external field at high frequencies, consequently the dielectric constant is due to the contribution from the lattice polarization [26]. This

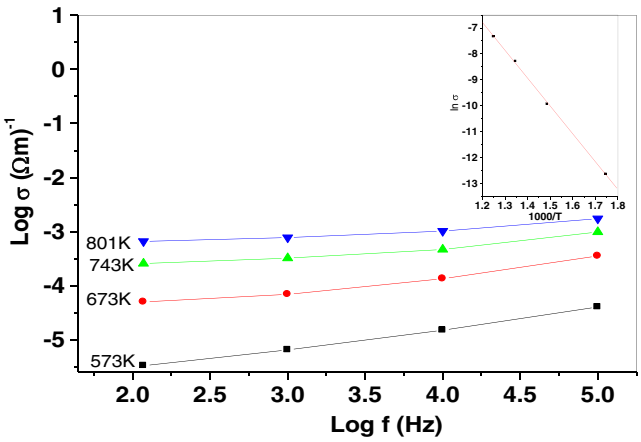

Fig. 8 Double logarithmic plot of ac conductivity vs. frequency at various temperatures for the HT874 sample. The inset shows the ($\ln\sigma_{ac}$) vs. (1000/T) at 120 Hz

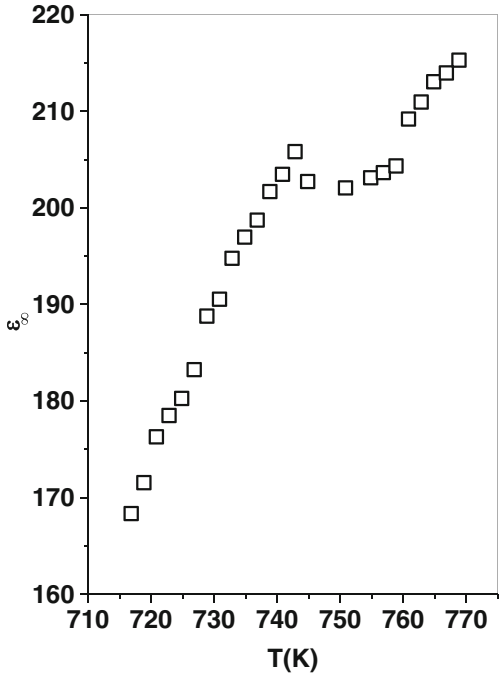

Fig. 9 The temperature dependence of high frequency dielectric constant ε_∞ for the HT874 sample

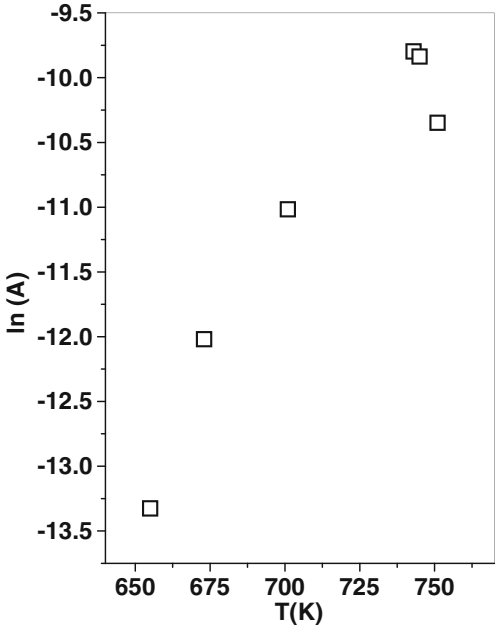

Fig. 11 The temperature dependence of the prefactor A(T) showing a peak at T_c for the HT874 sample

linear decrease occurs in the low frequency region and a frequency-independent plateau region at high frequencies as shown in (Fig. 7 (a)). At high temperatures the charge carrier term $\left[a_0(T)/\varepsilon_0 \sin(n(T)\pi/2)\omega^{n(T)-1}\right]$ becomes more and more prominent, thus resulting in the dielectric dispersion at low frequency [26, 33]. The presence of an anomalously strong dispersion of ε_r' near T_c suggests the coupling between the lattice and the charge carriers [26, 31]. The behavior of the ε_r'' in this sample in the low frequency and in the high temperature region can be explained by Eq. 4. In such circumstances the dc electric conductivity contribution is dominant, which is consistent with the data shown in (Fig. 7 (b)) [26, 32]. The ε_∞ value was selected as the dielectric constant obtained at 100 kHz, as the small dispersion around this frequency is negligibly. This may be attributed to the presence of an anomaly in the range of T_c. Figs. 9, 10 and 11 show the variation of the ε_∞, n(T) and A(T), with temperature respectively. From these Figs. it can be seen that the lattice contribution, ε_∞, shows a peak at T_c. The exponent n(T) decreases with increase in temperature and shows a minimum at T_c and then increases with further

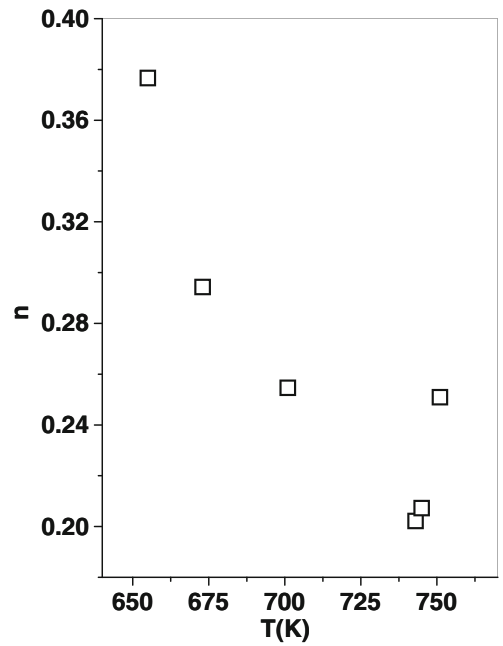

Fig. 10 Variation of the critical exponent n(T) with temperature showing a minimum at T_c of SBN for the HT874 sample

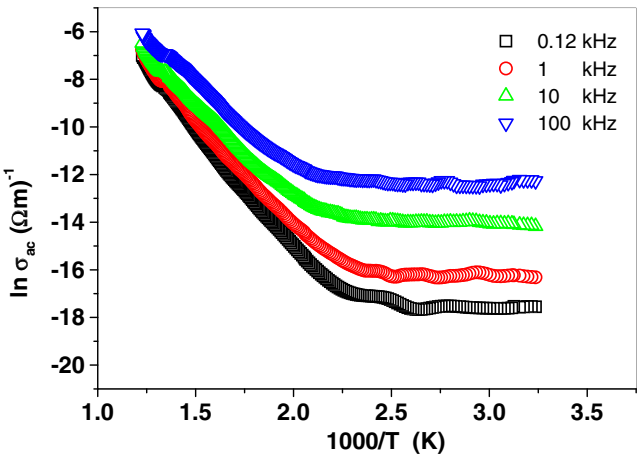

Fig. 12 Ac conductivity ($\ln\sigma_{ac}$) vs. (1000/T), at different frequencies for the HT874 sample

increase in temperature. The minimum observed at T_c can be attributed to the interaction of the charge carriers with the lattice. On the other side, the prefactor A(T), which is used to determine the strength of polarizability, exhibits a sharp peak at T_c. These above results are in line with those reported for ferroelectric $SrBi_2Nb_2O_9$ ceramics by B. H. Venkataraman et al. [26].

3.5 AC conductivity

The reciprocal temperature dependence of the ac conductivity as a function of temperature for the heat-treated (874 K/6 h) sample at various frequencies is shown in Fig. 12. From this Fig. it can be seen that the ac conductivity exhibits anomalous behavior at a particular temperature. The change in slope at a particular temperature which corresponds to the transition temperature in the sample obtained from the temperature dependence of the dielectric constant (Fig. 5). The change in slope of curve (Fig. 12) will reflect a change in the ac conductivity phenomenon in paraelectric and ferroelectric regions [8, 34]. At low temperatures, the ac conductivity is seen to be almost independent of temperature but shows different values at different frequencies indicating that major contribution to the conductivity result from the presence of space charges [35]. As the temperature increases, the ac conductivity shows an increase in curve tending to merge at high temperatures [35]. From the above results we concluded that the $SrBi_2Nb_2O_9$ embedded in a 50 % $Li_2B_4O_7$ glass matrix is not perfectly stoichiometric, but contains a certain amount of defects (e.g. oxygen vacancies) resulting from the volatilization of Bi_2O_3 at high temperatures [35, 36]. When Bi_2O_3 is lost, bismuth and oxygen vacancy complexes are formed in the $(Bi_2O_2)^{2+}$ layers. As frequency decreases, oxygen vacancies become active and mask the growth of the ferroelectric phase and hence no clear anomalies appear in the temperature dependence of the ac conductivity [35].

4 Conclusions

Ferroelectric $SrBi_2Nb_2O_9$ (SBN) embedded in a 50 % $Li_2B_4O_7$ glass matrix were successfully synthesized by heat treating the as-prepared sample. An $SrBi_2Nb_2O_9$ orthorhombic structure with $A2_1am$ space group was identified by Rietveld method. Ferroelectric $SrBi_2Nb_2O_9$ embedded in a $Li_2B_4O_7$ glass matrix have been found to exhibit strong low frequency dielectric dispersion when the studies were made in the 120 Hz–10 kHz frequency range at various temperatures. The parameters A(T) and n(T) are determined. An anomaly in the paraelectric–ferroelectric transition region is observed for both parameters near T_c indicating a coupling between the charge carriers and the phonons. From the ac conductivity plots it was observed that the electrical conductivity obeyed the universal power law dependence in accordance with the Jonscher's model.

References

1. H. Irie, M. Miyayama, T. Kudo, J. Appl. Phys. **90**, 4089–4094 (2001)
2. I. Coondoo, A.K. Jha, S.K. Agarwal, J. Eur. Ceram. Soc. **27**, 253–260 (2007)
3. S. Jesse, B.J. Rodriguez, S. Choudhury, A.P. Baddorf, I. Vrejoiu, D. Hesse, M. Alexe, E.A. Eliseev, A.N. Morozovska, J. Zhang, L.Q. Chen, S.V. Kalinin, Nat. Mater. **7**, 209 (2008)
4. N.S. Prasad, K.B.R. Varma, Mater. Sci. Eng. **B90**, 246 (2002)
5. J.-J. Shyu, C.-H. Chen, Ceram. Int. **29**, 447 (2003)
6. M.V. Shankar, K.B.R. Varma, J. Non-Cryst. Solids **226**, 145 (1998)
7. E.K. Abdel-Khalek, A.A. Bahgat, Phys. B **405**, 1986 (2010)
8. E.K. Abdel-Khalek, Shaaban, M. Salem, M. Farouk, E.A. Mohamed, I. Kashif, J. Non-Cryst. Solids **357**, 864 (2011)
9. M.V. Shankar, K.B.R. Varma, G.N. Subbanna, Mater. Res. Bull **31**, 475 (1996)
10. T.C. Chen, C.L. Thio, S.B. Desu, J. Mater. Res. **12**(10), 2628 (1997)
11. R.E. Newnham, R.W. Wolf, J.F. Dorrian, Mater. Res. Bull **6**, 1029 (1971)
12. K. Majhi, K.B.R. Varma, J. Non-Cryst. Solids **354**, 4543 (2008)
13. A. Marrota, A. Buri, Thermochim. Acta **40**, 397 (1980)
14. C. Karthik, K.B.R. Varma, J. Non-Cryst. Solids **353**, 1307 (2007)
15. E.C. Subba Rao, J. Am. Ceram. Soc. **45**, 166 (1962)
16. B.J. Ismunandar, J. Kennedy, Solid State Chem. **126**, 135 (1996)
17. N. Syam Prasad, G.N. Subbanna, K.B.R. Varma, Mater. Lett. **47**, 11 (2001)
18. F.A. Khalife, H.A. El Batal, A.A. Zooz, Ind J Pure Appl Phys **36**, 314 (1998)
19. M.R. Reddy, S.B. Raju, N. Veeraiah, J. Phys. Chem. Solids **61**, 1567 (2000)
20. A.F.L. Almeida, I.F. Vasconcelos, M.A. Valente, A.S.B. Sombra, Phys. B **322**, 276 (2002)
21. E. Kamitsos, M. Karakassides, G. Chryssikos, J. Phys. Chem. **91**, 1073 (1987)
22. G. Lakshminarayana, S. Buddhudu, Spectrochimica Acta Part A **63**, 295 (2006)
23. T. Friessnegg, S. Aggarwal, R. Ramesh, B. Nielsen, E.H. Poindexter, D.J. Keeble, Appl. Phys. Lett. **77**, 127 (2000)
24. A. Chen, Y. Zhi, L.E. Cross, Phys. Rev. B **62**, 228 (2000)
25. K.S. Rao, D.M. Prasad, P.M. Krishna, B.H. Bindu, K. Suneetha, J. Mater. Sci. **42**, 7363 (2007)
26. B. Harihara Venkataraman, K.B.R. Varma, Solid State Ion. **167**, 197 (2004)
27. Z. Lu, J.P. Bonnet, J. Ravez, P. Hagenmuller, Solid State Ion. **57**, 235 (1992)
28. T.A. Nealon, Ferroelectrics **76**, 377 (1987)
29. A.K. Jonscher, R.M. Hill, C. Pickup, J. Mater. Sci. **20**, 4431 (1985)
30. L. Zhigao, J.P. Bonnet, J. Ravez, P. Hagenmuller, Solid State Ion. **57**, 235 (1992)
31. A.K. Jonscher, *Dielectric relaxation in solids* (Chelsea Dielectric Press, London, 1983)
32. D. Kajewski, Z. Ujma, J. Phys. Chem. Solids **71**, 24 (2009)
33. Z. Lu, J.P. Bonnet, J. Ravez, P. Hagenmuller, Eur. J. Solid State Inorg. Chem. **28**(2), 363 (1991)
34. K. Sambasiva Rao, D. Madhava Prasad, P. Murali Krishna, B. Tilak, K.C. Varadarajulu, Mater. Sci. Eng., B **133**, 141 (2006)
35. I. Coondoo, A.K. Jha, S.K. Agarwal, J. Eur. Ceram. Soc. **27**, 253 (2007)
36. B.H. Park, S.J. Hyun, S.D. Bu, T.W. Noh, J. Lee, H.D. Kim, T.H. Kim, W. Jo, Appl. Phys. Lett. **74**, 1907 (1999)